

A Coating Strategy for Coevolving Photocatalysis to Stabilise Visible-Light Absorbing Semiconductors

Tianshuo Zhao

Yale University <https://orcid.org/0000-0003-3952-7603>

Rito Yanagi

Yale University

Yijie Xu

Yale University <https://orcid.org/0000-0002-0807-8262>

Yulian He

Yale University

Yuqi Song

Yale University

Meiqi Yang

Yale University

Shu Hu (✉ shu.hu@yale.edu)

Yale University <https://orcid.org/0000-0002-5041-0169>

Article

Keywords: coevolving photocatalysis, visible-light absorbing semiconductors, conformal coatings, cocatalysts energetic properties

Posted Date: September 23rd, 2020

DOI: <https://doi.org/10.21203/rs.3.rs-78917/v1>

License:  This work is licensed under a Creative Commons Attribution 4.0 International License.

[Read Full License](#)

Abstract

Semiconductors of narrow bandgaps and high quantum efficiency have not been successfully utilised for coevolving photocatalysis despite the widely demonstrated protective coating schemes. Herein, we showcase a general strategy of using conformal coatings and cocatalysts energetic properties to transform CdS powders and GaInP₂ films into stable and efficient photocatalysts for coevolution of H₂ and reversible redox couples. A scalable redox-mediated solar water-splitting reactor was constructed, regenerating the redox mediators while evolving O₂ in a separate compartment. Distinct from the single direction of charge transfer found with conventional photoelectrode stabilisation, the coating herein allows both photo-excited electrons and holes to spatially separate and inject simultaneously to the respective reductive and oxidative sites. With TiO₂ stabilisation, CdS particles produced H₂ continuously for 150 hours. Under simulated sunlight, solar-to-hydrogen (STH) efficiency of 5.9% and 9.4% can be achieved for the CdS and GaInP₂ panels, respectively, by stacking multiple panels and matching the rate of redox regeneration to that of H₂ production.

Main Text

Particulate photocatalysis is a promising platform for sunlight-driven hydrogen production and CO₂ reduction at scale.¹⁻⁵ Although recently particulate photocatalysts have attained nearly 100% quantum efficiency,⁶ their state-of-the-art solar-to-hydrogen (STH) conversion efficiency, including those of oxides,^{5,7} oxynitrides,^{8,9} and oxysulphides,¹⁰ remains around 1%.¹¹ An alternative direction is to utilise narrow bandgap semiconductive photoabsorbers, such as those II-V and III-V semiconductors, that are known for strong optical absorption, high quantum efficiency, and long carrier lifetime.¹²⁻¹⁴ For example, cadmium sulphide (CdS) and gallium-indium-phosphide (GaInP₂) photoabsorbers have bandgaps of 2.42 eV and 1.87 eV, respectively, promising >10% STH efficiency.^{1,15} However, these semiconductors suffer from poor photo-stability in water, and their few-hour stability is much shorter than the thousands of hours operation by oxides.⁵ Hole scavengers leverage their fast and irreversible kinetics to compete against photooxidation.¹⁶ These scavengers provide the chemical bias to improve H₂-evolution rates, but they cannot be regenerated to sustain continuous photocatalysis.

Existing coatings were shown to protect photoelectrodes for either reductive or oxidative reactions, but not for hosting both reactions simultaneously.¹⁷ Herein, we found the oxide coatings form a heterojunction, not a Schottky barrier, with the underlying protected semiconductors. Therefore, we developed a general approach to improve the stability and at the same time, to facilitate efficient charge separation and to transfer electrons and holes simultaneously during coevolving photocatalysis. Corroborated by both energetic measurements and numerical calculations, the charge separation was found driven by a semiconductor/coating/cocatalyst structure with locally varying barrier heights, rather than the specific morphology or crystal facets of the photocatalyst. As illustrated in **Figure 1a**, CdS particulate films and GaInP₂ epitaxial films were coated by TiO₂, the surfaces of which were subsequently

loaded with Rh cocatalysts (see Methods). This simple two-step procedure transformed narrow-bandgap semiconductors into stable photocatalysts: the CdS/TiO₂/Rh@CrO_x panel continuously evolved H₂ at 50.4 μmol h⁻¹ cm⁻², and showed an internal quantum yield (IQY) of 44.3% at 438 nm in a Na₂S solution. The GaInP₂/TiO₂/Rh@CrO_x panel achieved an H₂-evolution rate of 144.7 μmol h⁻¹ cm⁻², equivalent to a photocurrent density of 7.8 mA cm⁻². While the TiO₂ surface oxidised the reversible sulphide/polysulphide (S²⁻/S_n²⁻) redox couples, the Rh-core and CrO_x-shell, i.e. Rh@CrO_x, cocatalysts evolved H₂ and suppressed the re-reduction of redox mediators. The CrO_x shell also prevented performance degradation and sulphur poisoning of the Rh cocatalysts.

Stability of the coating-stabilised photocatalysts

A film of drop-casted CdS particles was encapsulated by TiO₂ *via* atomic-layer deposition (ALD) (**Fig. 1a**, inset). Then, the ALD TiO₂ was decorated with Rh@CrO_x core-shell cocatalysts *via* photodeposition (see Methods). This cocatalyst-decorated coating not only suppresses photocorrosion of the CdS semiconductor but also allows coevolution of H₂ and reversible redox mediators. In this case, photo-excited electrons and holes simultaneously inject to the active sites of Rh cocatalysts and bare TiO₂ surfaces, respectively, to drive the hydrogen evolution reaction (HER) and sulphide oxidation reaction (SOR) along the photocatalyst-liquid interface. It is necessary to capture hole charges by the reversible redox mediators (A/A⁻) to sustain overall water splitting, but it is also challenging due to their reversible kinetics. In this work, we mainly focus on the reversible SOR based on the sulphide/polysulphide (S²⁻/S_n²⁻) redox mediators in alkaline pH, but it can be extended to other redox mediators, e.g., IO³⁻/I⁻, [Fe(CN)₆]^{3-/4-}, and Fe^{3+/2+} in various pH.¹⁸⁻²⁰

CdS photocatalysts are known to rapidly degrade due to photooxidation of lattice sulphides, which forms soluble sulphates or insulating sulphur.²¹ Typical CdS photocatalysts were reported to evolve H₂ that lasted for only a few hours.^{22,23} Therefore, we tested the stability of TiO₂-stabilised CdS panel by measuring the cumulative amount of H₂ evolved in 50 mM Na₂S solutions (pH 13.0) over time (see Supplementary **Fig. S1**, Note 1, and Video 1). As shown in **Fig. 1b**, the CdS/3-nm TiO₂/Rh@CrO_x panel produced 1-atm H₂ for 150 hours continuously. To simplify the testing procedure, the redox solution was replenished by a new Na₂S solution every 8 – 9 hours without disturbing the measurement. In comparison, the bare CdS panel produced H₂ at a much lower rate while the activity dropped to almost zero after 10 hours. The lack of TiO₂ coating made the CdS powder film delaminate even during the Rh photodeposition. The X-ray photoelectron spectroscopy (XPS) Cd 3d and S 3p core-level spectra showed little changes after 150 hours (Supplementary **Fig. S2**). The absence of SO_x signature suggested that the TiO₂ coating eliminated the primary failure mode of CdS photocorrosion. The H₂-production activity decreased by 20% and 30% after the first 100 h, and 150 h, respectively, which was not due to the loss of CdS particles (Supplementary **Fig. S3** and Note 1).¹⁰ In another compartment, (photo-)electrochemical

redox-mediator reduction and water oxidation are paired with the H₂ photocatalysis to complete overall water splitting (see the Photocatalytic reactor Section).

Design for efficient charge separation and product coevolution

The introduction of coatings and cocatalysts improved the photocatalytic activity of CdS and GaInP₂. The commercial CdS powder film showed a 1-atm H₂-evolution rate of only 2.2 μmol h⁻¹ cm⁻² in a 100 mM Na₂S solution. The rate increased by a factor of 1.3 and 5.8, respectively, after coating 3 nm of TiO₂ only and after loading 1 wt% Rh on the TiO₂ (**Fig. 2a**). Upon growth of CrO_x shells on individual Rh nanoparticles, a significant boost for the activity to 50.4 μmol h⁻¹ cm⁻² was achieved. Similar improvement was observed with the GaInP₂ panel. With 3-nm TiO₂ and Rh@CrO_x deposition, the n-type GaInP₂ film evolved 1-atm H₂ at 144.7 μmol h⁻¹ cm⁻² in the Na₂S solution, 11 times of the as-grown GaInP₂ (**Fig. 2b**). This H₂-evolution rate was stable, while the bare GaInP₂ dropped to 28.8% of the initial rate within the first 1.5 hours. To our knowledge, this is the first demonstration of coevolving GaInP₂ photocatalysts. The equivalent photocurrent density of 2.7 and 7.8 mA cm⁻² was achieved by the TiO₂-stabilised CdS and GaInP₂ panels, respectively. Besides S²⁻/S_n²⁻, coevolution of H₂ and [Fe(CN)₆]^{3-/4-} redox couples by the CdS/TiO₂/Rh@CrO_x panel was also observed in a 50 mM K₄Fe(CN)₆ aqueous solution at pH 7.0 (Supplementary **Fig. S4**), showing the versatility of this coating strategy. The rate can be further improved by tuning the coating energetics and making facile charge transfer to redox mediators in future studies.^{24,25}

Efficient charge separation, leading to the simultaneous injection of electrons and holes to the liquid, can be realised through the varying barrier heights along the same photocatalyst-liquid interface. Cocatalyst deposition introduces two types of sites, i.e., semiconductor/TiO₂ and semiconductor/TiO₂/Rh@CrO_x, when in contact with the redox-mediator solution. We investigated their barrier-height energetics through light-intensity dependent OCP measurements by using CdS particle-assembled electrodes and GaInP₂ planar electrodes (see Methods).²⁶ The ohmic back contact for the CdS and GaInP₂ electrodes allows for probing of the averaged electrochemical potentials of photo-excited electrons. **Fig. S5a** shows that as the light intensity increased, the OCPs of the CdS/TiO₂ electrode measured in a 10 mM Na₂S solution (pH 12) became increasingly negative and reached a steady-state value of 0.34 V vs. RHE, denoted as OCP_{light}. The OCP_{light} shifted to -0.09 V vs. RHE after loading the CdS/TiO₂ electrode with Rh@CrO_x (**Fig. 3a**), indicating a reducing potential for the Rh@CrO_x sites to drive H⁺ reduction. The OCP_{light} of the CdS/TiO₂/RhCrO_x electrode was consistent with the conduction band (CB) edge position of the CdS/TiO₂ sites, which was determined from the Mott-Schottky analysis independently (Supplementary **Fig. S5b** and Note 2). Therefore, both sites are able to coevolve HER and SOR, according to their band edge positions (Supplementary **Fig. S6**).

Purging the redox solution with H₂ resembles the local environment during H₂-evolving photocatalysis. When multiple charge transfer pathways coexist at the photocatalyst-liquid interface, e.g., a two-redox

liquid junction, the OCP is the potential at the detailed balance of the kinetic rates for all the forward and backward charge-transfer pathways.²⁶ Unlike the almost unaltered OCPs of the CdS/TiO₂ electrode after H₂ purging (Supplementary **Fig. S5a**), the OCP_{dark} of CdS/TiO₂/Rh@CrO_x approached 0 V vs. RHE, while the OCP_{light} remained at - 0.10 V vs. RHE (**Fig. 3a**). In other words, the potential of the Rh cocatalysts (inside CrO_x shells) shifted upwards to align with $E^0(\text{H}^+/\text{H}_2)$. Meanwhile, the CdS CB position stayed at - 0.10 V vs. RHE. Instead of a fixed value, the barrier height at those CdS/TiO₂/Rh@CrO_x sites was reduced to 0.11 V, much smaller than the CdS/TiO₂ barrier height of 0.60 V (Supplementary Note 2). The variable barrier height of Rh nanoparticles is not specific but rather general for many nanoparticulate cocatalysts: they were typically photodeposited over a hydrous or electrolyte-wetted TiO₂ surface, thus applicable to our coevolution coating strategy.^{26,27} Following the same procedure, we obtained electron barrier heights of 0.68 V and 0.14 V for the GaInP₂/TiO₂ and GaInP₂/TiO₂/Rh@CrO_x liquid interface, respectively (Supplementary **Fig. S5c,d** and Note 2).

Our strategy achieves local charge separation without leveraging the barrier-height difference specific to crystal facets.^{6,28} Both photocatalysts feature a barrier-height difference, or asymmetric barrier energetics.²⁹ As illustrated in **Fig. 3b** and **3c**, the barrier-height difference induced an electric field between the HER and SOR sites. This field made photogenerated electrons transport to the Rh@CrO_x sites for H₂ evolution, whereas holes transport to and accumulated at the bare TiO₂ surface to oxidise the redox mediator. The detailed calculation for the band diagram is explained in the Supplementary Note 2 and **Fig. S7**, and the various energetic parameters are summarised in Supplementary Table S1.

However, only decorating Rh cocatalysts but without regulating the re-reduction of redox mediators cannot achieve sufficient barrier-height difference. The OCP_{light} of CdS/TiO₂/Rh electrodes, i.e., the Rh potential, was not raised to more negative potentials (**Supplementary Fig. S8**). As a two-redox liquid junction,²⁶ the Rh site could also transfer electrons to S_n²⁻/S²⁻: this process was fast enough to compete with the desirable pathway of H⁺ reduction. The resulting 0.45 V barrier height of the Rh sites was comparable to that of the CdS/TiO₂ sites. Therefore, this lack of energetic asymmetry adversely affected the charge separation efficiency for semiconductor/TiO₂/Rh panels without the CrO_x selectivity shell layer (**Fig. 2**). Besides, the selective Rh@CrO_x cocatalysts ensure the high activities regardless in 1-atm Ar, air, or H₂ atmospheres (Supplementary **Fig. S9**). Such high selectivity against O₂ reduction or S_n²⁻ reduction is consistent with the unchanged OCP_{light} at ca. - 0.10 V vs. RHE for the semiconductor/TiO₂/Rh@CrO_x panels. The continuous H₂ production eventually replaces the headspace with 1-atm H₂. Essentially, the observed activity trends highlighted the dual functionality of the Rh@CrO_x cocatalysts: i) improving kinetics and ii) creating barrier-height asymmetry to facilitate charge separation.

Modelling of steady-state charge separation

So far, the HER and SOR sites have been proven to bear different barrier heights. Therefore, we choose the CdS photocatalyst to build a semiconductor model and to simulate a steady-state distribution of photo-

excited electrons and holes in two dimensions, i.e., inside the CdS particle and along the TiO₂-liquid interface. The materials and junction properties used are discussed in Supplementary Note 3 and listed in Table S2. The CdS/TiO₂ solid-solid interface is modelled as a heterojunction. The barrier-height energetics vary along the liquid junction dynamically during H₂ photocatalysis: for simplicity, fixed Schottky barriers of 0.11-V and 0.60-V barrier height were set to simulate those HER and SOR sites, respectively. Their geometric parameters used in the simulation were estimated from **Fig. S10 – S11**.

The gradient of electron potential energy within the CdS indicated the steady-state electron-hole separation. A uniform carrier generation rate of ca. cm⁻³ s⁻¹ was calculated under 1-sun illumination (see Methods). **Fig. 3d** shows that the electron potential energy reached the maximum at the SOR sites and the minimum at the HER sites. Driven by this potential gradient, the simulated electron and hole transport directions, indicated by the red and black arrows, respectively, were consistent with the 1D schematic in **Fig. 3b**. From the HER and SOR site at the liquid interface into the CdS bulk, ca. 200 nm or 20% of the absorber volume was under an electric field (Supplementary **Fig. S12a – 12c**). Within this volume, either the electron or hole current dominated the total currents (Supplementary **Fig. S12d**). Away from the surface, electron diffusion current became comparable to and eventually higher than the electron drift current (Supplementary **Fig. S12e**). This spatial distribution indicated a steady-state electron accumulation at the Rh@CrO_x site (Supplementary **Fig. S12f**). Essentially, this diffusion-controlled charge separation is distinctive to the drift-dominated regime typically observed in solid-state energy conversion:³⁰ even a barrier-height difference much less than the bandgap enables efficient charge separation during coevolution.

Too thick TiO₂ coatings may reduce the hole injection rates, and thus, affect charge separation efficiency and photocatalytic activity. Experimentally, we observed that H₂ rates of the CdS photocatalyst decreased dramatically when the TiO₂ thickness reached 10 nm (Supplementary **Fig. S13**). This thickness-dependent behaviour should not always occur but was attributed to the energetic mismatch during hole transport from CdS to the redox mediator. Through > 3-nm thick TiO₂, the hole hopping transport was slow as compared to the direct tunnelling transport,³¹ because the Ti³⁺-defect band does not match with the energy level of CdS valence bands. In the modelling, different charge injection currents can be simulated by modulating the hole surface recombination velocity (SRV) at the 10-nm TiO₂. The modelling outcome is consistent with the measured activity: reducing the hole SRV by 10 times decreased the photocurrent, or the H₂-evolution rate, to a third of the 3-nm TiO₂ coated photocatalyst (Supplementary **Fig. S13**). The calculated effective resistivity of ~ 10⁸ Ω for the 10-nm TiO₂ layer also agrees with the literature report.³¹ The low SRV led to significant hole accumulation up to 10²¹ cm⁻³ at the 10-nm TiO₂ surface (Supplementary **Fig. S14**). Therefore, more carrier recombination occurred inside the CdS than with 3-nm TiO₂ coatings, reducing the photocurrents adversely. Insufficient hole transport that causes activity degradation is irrespective to CdS carrier lifetime or radiative efficiency.

Improving quantum yields of CdS photocatalysts

With 3-nm TiO₂, 1 wt% of Rh, and 1 wt% Cr loading, one CdS photocatalytic panel produced H₂ at a rate of 50.4 μmol h⁻¹ cm⁻² in a 100 mM Na₂S solution (pH 13.5) (see Methods). We measured an apparent quantum yield (AQY) of 24.6% at 438 nm for the same panel in the 100 mM Na₂S solution. Considering 55.5% of the light absorbed at that wavelength (Supplementary **Fig. S15**), the internal quantum yield (IQY) of the panel was calculated to be 44.3%. Stacking multiple panel devices can take full advantage of the incident light. With a three-panel stacking, the H₂ evolution rate increased to 90.6 μmol h⁻¹ cm⁻¹, and the AQY reached 44.2%, approaching the IQY (Supplementary **Fig. S16** and Video 2). This H₂ rate promises STH efficiency of 5.9% in a redox-mediated solar H₂ generator.

The numerical simulation also helped us discover the property that limited the measured IQY to be 44.3%. Experimentally, we obtained a CdS carrier lifetime of 0.1 ns (Supplementary **Fig. S17a**), which is short. Using the experimental lifetime, we introduced Shockley-Read-Hall recombination in the model (see Methods) to show that 44.0% of photo-excited electrons are collected as photocurrents. Varying the modelling parameter further showed the possibility of reaching 90% IQY, as long as the carrier lifetime of commercial CdS powders could be longer than 0.5 ns (Supplementary **Fig. S17b**). Such sensitivity to the carrier lifetime is consistent with the diffusion-controlled charge separation driven by a small barrier-height asymmetry. Therefore, increasing the carrier diffusion length or the depletion region volume is desirable (Supplementary Note 4),²⁹ and can follow various reported strategies.³²

Photocatalytic reactor

We constructed a solar-fuel generator, which allows for H₂ and O₂ evolution at two separated reactor chambers continuously, or at two separated times. As illustrated in **Fig. 4a**, a photocatalysis (PC) reactor was integrated with a photovoltaic-driven electrolysis (PVE). The reversible S²⁻/S_n²⁻ redox mediators shuttle photogenerated hole charges between the PC reactor and PVE device. A triple-junction (3-J) amorphous Si (*a*-Si) solar cell of 1.7 – 2.0 eV bandgaps absorbs the light transmitted through the CdS panel, to power the redox regeneration at a matching current.³³ This proof-of-concept redox-mediated water-splitting reactor was constructed for simplicity.^{34,35} For the redox-mediator regeneration, the PVE component can be essentially replaced by a suspension or a panel of particulate photocatalysts:³⁶ e.g., the iron-, cobalt-, and iodine-mediated O₂ evolution by BViO₄ and WO₃ photocatalysts.^{20,37,38} More generally, the GaInP₂/TiO₂/Rh@CrO_x panel can also operate inside the H₂-evolving chamber when a GaInP₂ epi-layer is lifted-off from reusable GaAs substrates and mounted on a glass panel.³⁹ The light transmitted through the GaInP₂ layer can drive redox regeneration.

Fig. 4b shows a separated production of stoichiometric H₂ and O₂ by alternating the PC and the PVE processes. The amount of H₂ evolved was directly measured by an online gas chromatograph (GC), while the amount of O₂ was quantified based on the charge passed and the 100% Faradaic efficiency of IrO_x catalysts (see Methods). The membrane-electrode electrolysis device consists of a Pt/C catalyst-loaded cathode and an IrO_x/C catalyst-loaded anode. The cathode reduces S_n²⁻ ions to regenerate S²⁻, whereas

the anode produces O_2 and protons by oxidising pure water. A cation exchange membrane (CEM) prevents the O_2 crossover, while replenishing the redox solution with the protons needed for H_2 evolution. In the PC step, $115.3 \mu\text{mol}$ of H_2 was evolved under 1-sun illumination at 1 atm, equivalent to 22.2 C of charges received by the reversible S^{2-}/S_n^{2-} redox mediators. In the second PVE step, the same amount of charge was passed to the electrolysis device. This step generated $57.7 \mu\text{mol}$ of O_2 , i.e., a 2:1 molar ratio of H_2 and O_2 . For this demonstration, the $25.6 \mu\text{mol h}^{-1} \text{cm}^{-2}$ rate of H_2 evolution under 1-sun illumination indicated STH conversion efficiency of 1.7%, equivalent to a photocurrent of 1.4 mA cm^{-2} . The H_2 rate of $25.6 \mu\text{mol h}^{-1} \text{cm}^{-2}$ after two consecutive cycles was kept the same as in the first cycle, and the potential of the redox mediator solution also returned to the original open-circuit potential after each PVE regeneration (Supplementary Note 5 and **Fig. S18**). Both indicated complete regeneration of the redox mediators.

The rates of oxygen evolution and redox regeneration by the electrolysis device are further scalable. Thus, it is also reasonable to assume that all remaining sunlight transmitted through the CdS panel can be utilised to power the S^{2-}/S_n^{2-} regeneration at a rate matching to the H_2 production. In this case, the reactor should achieve STH conversion efficiency as high as 5.9% by stacking three CdS panels to maximise the light capture. Besides, the redox mediators buffer the photo-excited charges, such that the reactor operation can be flexibly tailored by using short-term energy storage, even with intermittent solar irradiation or diurnal solar cycles. A similar water-splitting reactor based on the TiO_2 -stabilised GaInP_2 panel can pair with efficient O_2 -evolving photocatalysts, such as stabilised GaAs or Si,²⁹ to utilise the transmitted light and regenerate redox mediators. The regeneration rate can match to that of the H_2 evolution by the GaInP_2 panel shown in **Fig. 2b**, achieving STH efficiency of 9.4%. Equivalently, 1-sun H_2 production rates of $4.8 \cdot 10^{-7}$ and $7.7 \cdot 10^{-7} \text{ kg s}^{-1} \text{m}^{-2}$ are achievable from coating-stabilised CdS and GaInP_2 , respectively, which meets the US Department of Energy MYRD&D 2020 target for dual bed photocatalytic systems with product separation.⁴⁰

Conclusions

This work demonstrates a general stabilisation strategy for coevolving photocatalysts by showcasing improved stability and charge separation efficiency of photocatalytic CdS and GaInP_2 panels protected by TiO_2 . The CdS/ TiO_2 /Rh@ CrO_x panel showed an AQY of 44.2% and 150 h of stable operation in reversible S^{2-}/S_n^{2-} redox solutions. The H_2 evolution rate of 90.6 and $144.7 \mu\text{mol h}^{-1} \text{cm}^{-1}$ achieved by coating-stabilised CdS panels and GaInP_2 panels is equivalent to reaching 5.9% and 9.4% STH conversion efficiency, respectively. The stability, H_2 rate, and AQY of the CdS and GaInP_2 panel set records for particulate water splitting (Supplementary Table S3). The current photocatalytic activity was limited by the intrinsic properties of CdS powders, not by the coating approach. Efficient charge separation and simultaneous injection of both types of carriers were induced by the asymmetric barrier heights between the local HER and SOR sites, which were nanometres apart and distributed along the liquid-junction

interface. This simple design is expected to initialise new development in water-splitting reactors, which produced stoichiometric and separated H₂ and O₂ gases. Future directions include (i) improving carrier lifetime of CdS particles, (ii) employing other reversible redox mediators and O₂-evolving photocatalysts to optimise the redox regeneration processes, and (iii) improving hole transport through >10-nm coatings.

Methods

Chemicals and materials. CdS powders were purchased from Nanoshel LLC (Delaware, USA). N-type GaInP₂ (100) with 500 nm thickness and $N_p = 1 - 2 \times 10^{17} \text{ cm}^{-3}$ grown on GaAs (100) wafers were purchased from University Wafer, Inc. Sodium hexachlororhodate (III) (Na₃RhCl₆), Potassium chromate (K₂CrO₄, >99.0%), Tetrakis(dimethylamido)titanium (IV) (TDMAT, 99.999%) were purchased from Sigma Aldrich. Anhydrous methanol (99.0%) and anhydrous sodium sulphide (Na₂S) were purchased from Alfa Aesar. Cadmium chloride (CdCl₂, 99.99%) was purchased from Acros Organics.

Fabrication of CdS/TiO₂ panels. CdS powders were treated by CdCl₂ before constructing photocatalytic panels. The CdCl₂ surface modification improved the optoelectronic properties of CdS. CdS powders (5 mg/mL) and CdCl₂ (10 mM) were mixed in methanol and sonicated for 10 min. Then the powders were dried by filtering through filter paper and evaporating the residue methanol at 80 °C to obtain CdCl₂ treated CdS. On a pre-cleaned (1 M HCl and DI water) frosted glass substrate (1.8x2.5 cm²), 10 mg of CdCl₂ treated CdS powders were added with 30 µL of methanol to form a slurry. A uniform film of powders was made via the roll press method with a glass rod. For the TiO₂ coating, CdS photocatalyst panels were placed in the ALD chamber and maintained at 150 °C. H₂O and TDMAT were pulsed alternatively into the chamber as the oxidising and titanium precursors, respectively. Once the desired number of cycles were reached, the ALD process was terminated, and the TiO₂-coated CdS panels were cooled down to room temperature for use.

Fabrication of GaInP₂/TiO₂ panels. The commercial GaInP₂ of 500 nm was grown on lattice-matched n⁺-GaAs (100) wafers with electron concentration of $1 - 2 \times 10^{17} \text{ cm}^{-3}$. A multi-layer metal contact was sputtered in the order of Ni/Au-Ge/Ag/Au with thickness of 5 nm/50 nm/50 nm/30 nm on the backside of the n⁺-GaAs. The substrate was annealed at 350 °C for 1 min to form ohmic contacts. A 2-min treatment in HF buffer was applied to remove surface oxide. Immediately following the HF treatment, the TiO₂ ALD is performed in the identical way as described above. Finally, copper wires were soldered to the back contact by indium and encapsulated by epoxy.

Photodeposition of Rh@CrO_x on CdS/TiO₂. For both photodeposition and photocatalytic reactions, we utilised a home-built photoreactor, which consists of a closed-loop glass manifold connected to a Gas Chromatograph (GC; SRI 8610C #3) via automatic sampling valves. The GC quantified the amount of gas produced with a molecular sieve column (MS-13X) and a thermal conductivity detector. Argon (Ar) was used as a carrier gas for the GC. The glass manifold was strictly sealed and airtight to ensure the vacuum

level of 1×10^{-2} Torr. A top-irradiation reaction vessel containing the photocatalyst and reactant solution was connected to the glass manifold with circulating cooling water to keep the reaction temperature at 10 °C. The system was degassed and purged with Ar to remove air; and a background pressure (Ar + water vapour) was adjusted to 100 Torr before each reaction. The irradiation at the sample was $\sim 340 \text{ mW cm}^{-2}$ generated from a 1000 W Mercury-Xenon Arc Lamp with an optical cutoff filter ($\lambda \geq 395 \text{ nm}$).

For photodeposition of cocatalysts, a TiO_2 -coated CdS panel was placed in a degassed mixture of 8 mL of DI water and 2 mL of methanol with 1 wt% of Rh from Na_3RhCl_6 . During the photodeposition, the amount of H_2 evolved was monitored by the GC every 30 min. The deposition was stopped after 1 – 1.5 hours as the H_2 -evolution rate became steady-state. Following the Rh deposition, the CrO_x shell was deposited in a similar approach, where 1 wt% of Cr from K_2CrO_4 was added to the mixture of DI water and methanol. Photodeposition of CrO_x typically lasted 2.5 – 3 hours depending on when the H_2 -evolution rate became steady. The 1 wt% of Rh and 1 wt% of Cr were found to be the optimal loading condition that yielded the highest H_2 -evolution rate.

Electrodeposition of Rh@ CrO_x on $\text{GaInP}_2/\text{TiO}_2$. To deposit Rh, the $\text{GaInP}_2/\text{TiO}_2$ photoelectrode was cyclically scanned three times from – 0.3 V to 0.1 V vs. Ag/AgCl in an N_2 -purged aqueous Na_3RhCl_6 solution (5 mg mL^{-1}). Then the CrO_x deposition was conducted in a 10 mg mL^{-1} K_2CrO_4 solution in DI water by applying a constant potential of – 1.0 V vs. Ag/AgCl for 5 hours under N_2 purging.

Photocatalytic reactions in the Na_2S solution. For a typical reaction, a CdS/ TiO_2 panel or $\text{GaInP}_2/\text{TiO}_2$ photoelectrode loaded with Rh@ CrO_x cocatalysts was immersed in 10 mL of Na_2S aqueous solution. An optimal activity was observed when the Na_2S concentration was 100 mM (pH 13.5), which was then used for all rate measurements. The effect of Na_2S concentration is still under investigation. The background pressure in the photoreactor was adjusted to be close to 760 Torr before the reaction began. A solar simulator (AAA-grade, Abet Technologies) with an AM 1.5 G filter was used as the illumination source. 1-sun illumination intensity was calibrated by a certified photodiode.

Quantum yield measurements. Photocatalytic H_2 evolution was performed twice with a 425 nm and a 450 nm long-pass filter (Edmund Optics) under AM1.5 G illumination, respectively. The corresponding H_2 evolution rates were obtained as $r_{\text{H}_2,425 \text{ nm}}$ and $r_{\text{H}_2,450 \text{ nm}}$. The rate at $438 \pm 12.5 \text{ nm}$ was then determined by $r_{\text{H}_2,438 \text{ nm}} = r_{\text{H}_2,425 \text{ nm}} - r_{\text{H}_2,450 \text{ nm}}$. AQY was calculated according to $\text{AQY} = 2 \times r_{\text{H}_2,438 \text{ nm}} \times N_A / A \cdot I_{438 \text{ nm}} / h\nu$, where N_A is Avogadro's number, A is the illuminated area, $I_{438 \text{ nm}}$ is light intensity at 438 nm, h is Planck's constant and ν is the photon's frequency at 438 nm. AM 1.5 G spectrum was used to calculate the $I_{438 \text{ nm}}$ by integrating the light intensity from 425 to 450 nm to count for spectral dependence.

Open-circuit potential (OCP) measurements. CdS powder-based photoelectrodes were made through the particle transfer method.⁴¹ 500 nm of Ti and 200 nm of Au were sputtered onto the CdS film as

conductive back contacts. Carbon tape attached to a glass substrate was then used to peel off the CdS particles covered by the metal layers. The electrode was then loaded into the ALD tool for TiO₂ deposition. Finally, the electrode was completed by contacting copper wires with the carbon tape and encapsulated by epoxy. The OCP measurements were conducted on a Bio-Logic S200 potentiostat with Ag/AgCl used as a reference electrode and a carbon rod as a counter electrode. All OCPs of the CdS powder electrode and GaInP₂ electrode were measured in 10 mM Na₂S solutions.

Electrochemical impedance spectroscopy (EIS) measurements. The CdS powder-based photoelectrode or GaInP₂ photoelectrode was measured in the aqueous [Fe(CN)₆]^{3-/4-} solution at pH 12 (50 mM K₃Fe(CN)₆ and 350 mM K₄Fe(CN)₆) in the complete dark. The impedance was measured from 10 kHz to 1 Hz and fitted with a Randles circuit to extract the capacitance of the liquid junction. In the Mott-Schottky plot, the intercept to the x-axis provided the flat-band potential, and the slope was used to calculate the doping concentration of the semiconductor.

Photovoltaic-electrolysis (PVE) device. Flex-stak PEM fuel cell (purchased from the Fuel Cell Store) was utilised to assemble the PVE device. Both the anodic and cathodic compartment were composed of a plastic end plate, a graphite plate and a home-made acrylic frame. A CEM separated the two compartments. Pt on carbon cloth (the Fuel Cell Store) was used as cathodic catalysts. IrO_x nanoparticles were synthesised and electrodeposited on carbon paper following a reported method.⁴² A 3-J *a*-Si solar panel placed in tandem with the photoreactor powered the PVE cell.

Faradic efficiency measurements. Faradaic efficiency (FE) was measured in an airtight cell with a three-electrode setup and two additional ports for carrier gas. The gas outlet was connected to the GC for analysing the gas products. Counter electrode (Pt wire) was separated from the cell by a Nafion 117 membrane. Ar carrier gas was continuously purged through the cell to the GC. The flow rate was kept constant (10 sccm) using a mass flow controller (MFC), which was calibrated using a bubble meter. The FE was determined by the ratio between the produced O₂ and the amount of passed charges on the OER catalysts. Following this method, we measured a ~ 100% FE for the IrO_x/C catalyst under chronopotentiometry at 1 mA.

Simulation of photocatalyst electrostatics Using the COMSOL Multiphysics Semiconductor Module, a 2D model was built for the CdS/TiO₂/Rh@CrO_x structure. The CdS was modelled as a semi-sphere of 1 μm in radius, which was conformally coated with a 3-nm TiO₂ layer. The Rh/CrO_x sites of 100 nm in length were distributed periodically on the surface. The length scale of Rh sites is such that their local barrier heights are not influenced by CdS/TiO₂ surroundings.⁴³ The energetics were simulated by solving the Poisson's Equation, drift-diffusion current, and continuity equations under open-circuit conditions. A heterojunction boundary condition was used for the CdS/TiO₂ interface. For liquid-junction interfaces, Schottky contacts were set for the TiO₂- and Rh@CrO_x-liquid sites with the barrier heights of 0.60 and 0.11 V for SOR and HER sites, respectively. The absorption coefficient of CdS is ~ 10⁵ cm⁻¹. Light can penetrate ~ 1 μm deep in the CdS. As a simplification, a generation rate of cm⁻³ s⁻¹ was introduced uniformly in the 1-μm CdS

to mimic 1-sun illumination. Shockley-Read-Hall recombination processes were imitated by setting electron trap states with 0.25 eV below the conduction band of CdS⁴⁴ for the energy level and cm^{-3} for the trap density in the model. For the IQY simulation, the generation rate was reduced to $\text{cm}^{-3} \text{s}^{-1}$, corresponding to the light intensity of $438 \pm 12.5 \text{ nm}$ spectra. The surface recombination velocity at the TiO_2 -liquid junction was varied to achieve a thermionic current that matches with the experimental result.

Materials characterisations. The SEM, AFM and TEM images were taken by a Hitachi SU8230 UHR system, a Cypher ES Environmental AFM system and an FEI Tecnai Osiris system (200 kV) equipped with EDS, respectively. X-ray photoelectron spectroscopy (XPS) measurements were conducted on the PHI VersaProbell. Diffused reflectance spectroscopy (DRS) of CdS panel was obtained on a UV-visible spectrometer (UV-2600, SHIMADZU). Time-resolved photoluminescence (TRPL) was collected using time-correlated single-photon counting (PicoHarp 300). The optical excitation was provided by a 480-nm pulsed laser, and the detection wavelength was centred at 550 nm with a 500 nm long-pass filter.

Declarations

Acknowledgements

The authors thank the start-up support from Yale Energy Sciences Institute. The authors thank Dr. Cheng Hua and Jake Heinlein for automation of the photoreaction measurements, Dr. Joerg Nikolaus for the timely help with the AFM measurements, Prof. Brudvig for supporting the UV-vis spectrometer, Junying Tang for preparing the IrO_x nanoparticles, and Xianbing Miao for setting up the Faraday efficiency apparatus. R.Y. acknowledges fellowship support from the Japan Student Services Organization. Y. X. thanks the Tsinghua University undergraduate overseas academic research support program.

Author information

Affiliations

Department of Chemical and Environmental Engineering, Yale University, New Haven, CT, USA

Tianshuo Zhao, Rito Yanagi, Yijie Xu, Yulian He, Yuqi Song, Meiqi Yang, and Shu Hu

Energy Sciences Institute, Yale University, West Haven, CT, USA

Tianshuo Zhao, Rito Yanagi, Yulian He, Meiqi Yang, and Shu Hu

Contributions

T. Z. and S. H. conceived the idea and designed the experiments. T. Z. and Y. X. developed the fabrication of the CdS photocatalytic panel. T. Z., R. Y. and Y. X. performed photoreactions and optimised the activity. Y. H. conducted the TEM and EDS characterisation. M. Y. measured the XPS. T.Z. performed the SEM. Y. S. fabricated the particle-assembled photoelectrode and measured electrochemical impedance spectra. R.

Y. helped T. Z. perform OCP measurements. T.Z. performed numerical simulations with R. Y.'s inputs. T.Z. assembled the water-splitting reactor with help from R. Y., and R.Y. measured FE. All authors discussed and analysed the data. T.Z., R. Y. and S.H. wrote and revised the manuscript.

References

1. Chen, S., Takata, T. & Domen, K. Particulate photocatalysts for overall water splitting. *Nat. Rev. Mater.* **2**, 17050 (2017).
2. Fabian, D. M. *et al.* Particle suspension reactors and materials for solar-driven water splitting. *Energy Environ. Sci.* **8**, 2825–2850 (2015).
3. AlOtaibi, B., Fan, S., Wang, D., Ye, J. & Mi, Z. Wafer-level artificial photosynthesis for CO₂ reduction into CH₄ and CO using GaN nanowires. *ACS Catal.* **5**, 5342–5348 (2015).
4. Osterloh, F. E. & Parkinson, B. A. Recent developments in solar water-splitting photocatalysis. *MRS Bull.* **36**, 17–22 (2011).
5. Goto, Y. *et al.* A particulate photocatalyst water-splitting panel for large-scale solar hydrogen generation. *Joule* **2**, 509–520 (2018).
6. Takata, T. *et al.* Photocatalytic water splitting with a quantum efficiency of almost unity. *Nature* **581**, 411–414 (2020).
7. Wang, Q. *et al.* Particulate photocatalyst sheets based on carbon conductor layer for efficient z-scheme pure-water splitting at ambient pressure. *J. Am. Chem. Soc.* **139**, 1675–1683 (2017).
8. Hsu, W.-P., Mishra, M., Liu, W.-S., Su, C.-Y. & Perng, T.-P. Fabrication of direct Z-scheme Ta₃N₅-WO_{2.72} film heterojunction photocatalyst for enhanced hydrogen evolution. *Appl. Catal. B Environ.* **201**, 511–517 (2017).
9. Yang, J.-H. *et al.* Highly enhanced photocatalytic water-splitting activity of gallium zinc oxynitride derived from flux-assisted Zn/Ga layered double hydroxides. *Ind. Eng. Chem. Res.* **57**, 16264–16271 (2018).
10. Wang, Q. *et al.* Oxysulfide photocatalyst for visible-light-driven overall water splitting. *Nat. Mater.* **18**, 827–832 (2019).
11. Wang, Q. & Domen, K. Particulate photocatalysts for light-driven water splitting: mechanisms, challenges, and design strategies. *Chem. Rev.* **120**, 919–985 (2020).
12. Kayes, B. M. *et al.* 27.6% Conversion efficiency, a new record for single-junction solar cells under 1 sun illumination. *2011 37th IEEE Photovoltaic Specialists Conference* 000004–000008 (IEEE, 2011).
13. Wallentin, J. *et al.* InP nanowire array solar cells achieving 13.8% efficiency by exceeding the ray optics limit. *Science* **339**, 1057–60 (2013).
14. Metzger, W. K. *et al.* Exceeding 20% efficiency with in situ group V doping in polycrystalline CdTe solar cells. *Nat. Energy* **4**, 837–845 (2019).
15. Garcia-Esparza, A. T. & Takanabe, K. A simplified theoretical guideline for overall water splitting using photocatalyst particles. *J. Mater. Chem. A* **4**, 2894–2908 (2016).

16. Yuan, Y.-J., Chen, D., Yu, Z.-T. & Zou, Z.-G. Cadmium sulfide-based nanomaterials for photocatalytic hydrogen production. *J. Mater. Chem. A* **6**, 11606–11630 (2018).
17. Hu, S. *et al.* Thin-film materials for the protection of semiconducting photoelectrodes in solar-fuel generators. *J. Phys. Chem. C* **119**, 24201–24228 (2015).
18. Qi, Y. *et al.* Inhibiting competing reactions of iodate/iodide redox mediators by surface modification of photocatalysts to enable Z-scheme overall water splitting. *Appl. Catal. B Environ.* **224**, 579–585 (2018).
19. Qi, Y. *et al.* Redox-based visible-light-driven Z-scheme overall water splitting with apparent quantum efficiency exceeding 10%. *Joule* **2**, 2393–2402 (2018).
20. Zhao, Y. *et al.* A hydrogen farm strategy for scalable solar hydrogen production with particulate photocatalysts. *Angew. Chemie* **132**, 9740–9745 (2020).
21. Ning, X. & Lu, G. Photocorrosion inhibition of CdS-based catalysts for photocatalytic overall water splitting. *Nanoscale* **12**, 1213–1223 (2020).
22. Li, Z. *et al.* Biomimetic electron transport via multiredox shuttles from photosystem II to a photoelectrochemical cell for solar water splitting. *Energy Environ. Sci.* **10**, 765–771 (2017).
23. Wolff, C. M. *et al.* All-in-one visible-light-driven water splitting by combining nanoparticulate and molecular co-catalysts on CdS nanorods. *Nat. Energy* **3**, 862–869 (2018).
24. Siddiqi, G. *et al.* Stable water oxidation in acid using manganese-modified TiO₂ protective coatings. *ACS Appl. Mater. Interfaces* **10**, 18805–18815 (2018).
25. Chen, X., Shen, X., Shen, S., Reese, M. O. & Hu, S. Stable CdTe photoanodes with energetics matching those of a coating intermediate band. *ACS Energy Lett.* **5**, 1865–1871 (2020).
26. Pan, Z. *et al.* Mutually-dependent kinetics and energetics of photocatalyst/co-catalyst/two-redox liquid junctions. *Energy Environ. Sci.* **13**, 162–173 (2020).
27. Lin, F. & Boettcher, S. W. Adaptive semiconductor/electrocatalyst junctions in water-splitting photoanodes. *Nat. Mater.* **13**, 81–86 (2014).
28. Li, R. *et al.* Spatial separation of photogenerated electrons and holes among {010} and {110} crystal facets of BiVO₄. *Nat. Commun.* **4**, 1432 (2013).
29. Pan, Z. *et al.* Elucidating charge separation in particulate photocatalysts using nearly intrinsic semiconductors with small asymmetric band bending. *Sustain. Energy Fuels* **3**, 850–864 (2019).
30. Chowdhury, F. A., Trudeau, M. L., Guo, H. & Mi, Z. A photochemical diode artificial photosynthesis system for unassisted high efficiency overall pure water splitting. *Nat. Commun.* **9**, 1707 (2018).
31. Scheuermann, A. G., Prange, J. D., Gunji, M., Chidsey, C. E. D. & McIntyre, P. C. Effects of catalyst material and atomic layer deposited TiO₂ oxide thickness on the water oxidation performance of metal–insulator–silicon anodes. *Energy Environ. Sci.* **6**, 2487 (2013).
32. Kim, W. D. *et al.* Role of surface states in photocatalysis: study of chlorine-passivated CdSe nanocrystals for photocatalytic hydrogen generation. *Chem. Mater.* **28**, 962–968 (2016).

33. Keene, S., Bala Chandran, R. & Ardo, S. Calculations of theoretical efficiencies for electrochemically-mediated tandem solar water splitting as a function of bandgap energies and redox shuttle potential. *Energy Environ. Sci.* **12**, 261–272 (2019).
34. Li, Z. *et al.* Air-breathing aqueous sulfur flow battery for ultralow-cost long-duration electrical storage. *Joule* **1**, 306–327 (2017).
35. Zhang, S. *et al.* Recent progress in polysulfide redox-flow batteries. *Batter. Supercaps* **2**, 627–637 (2019).
36. Pinaud, B. A. *et al.* Technical and economic feasibility of centralized facilities for solar hydrogen production via photocatalysis and photoelectrochemistry. *Energy Environ. Sci.* **6**, 1983 (2013).
37. Sasaki, Y., Kato, H. & Kudo, A. $[\text{Co}(\text{bpy})_3]^{3+/2+}$ and $[\text{Co}(\text{phen})_3]^{3+/2+}$ electron mediators for overall water splitting under sunlight irradiation using Z-scheme photocatalyst system. *J. Am. Chem. Soc.* **135**, 5441–5449 (2013).
38. Maeda, K., Higashi, M., Lu, D., Abe, R. & Domen, K. Efficient nonsacrificial water splitting through two-step photoexcitation by visible light using a modified oxynitride as a hydrogen evolution photocatalyst. *J. Am. Chem. Soc.* **132**, 5858–5868 (2010).
39. Geisz, J. F. *et al.* High-efficiency GaInP/GaAs/InGaAs triple-junction solar cells grown inverted with a metamorphic bottom junction. *Appl. Phys. Lett.* **91**, 023502 (2007).
40. US DOE Fuel Cell Technologies Office. *Fuel cell technologies program multi-year research, development, and demonstration plan.* (2015).
41. Minegishi, T., Nishimura, N., Kubota, J. & Domen, K. Photoelectrochemical properties of LaTiO_2N electrodes prepared by particle transfer for sunlight-driven water splitting. *Chem. Sci.* **4**, 1120 (2013).
42. Zhao, Y., Hernandez-Pagan, E. A., Vargas-Barbosa, N. M., Dysart, J. L. & Mallouk, T. E. A high yield synthesis of ligand-free iridium oxide nanoparticles with high electrocatalytic activity. *J. Phys. Chem. Lett.* **2**, 402–406 (2011).
43. Laskowski, F. A. L. *et al.* Nanoscale semiconductor/catalyst interfaces in photoelectrochemistry. *Nat. Mater.* **19**, 69–76 (2020).
44. Nicholas, K. H. & Woods, J. The evaluation of electron trapping parameters from conductivity glow curves in cadmium sulphide. *Br. J. Appl. Phys.* **15**, 783–795 (1964).

Figures

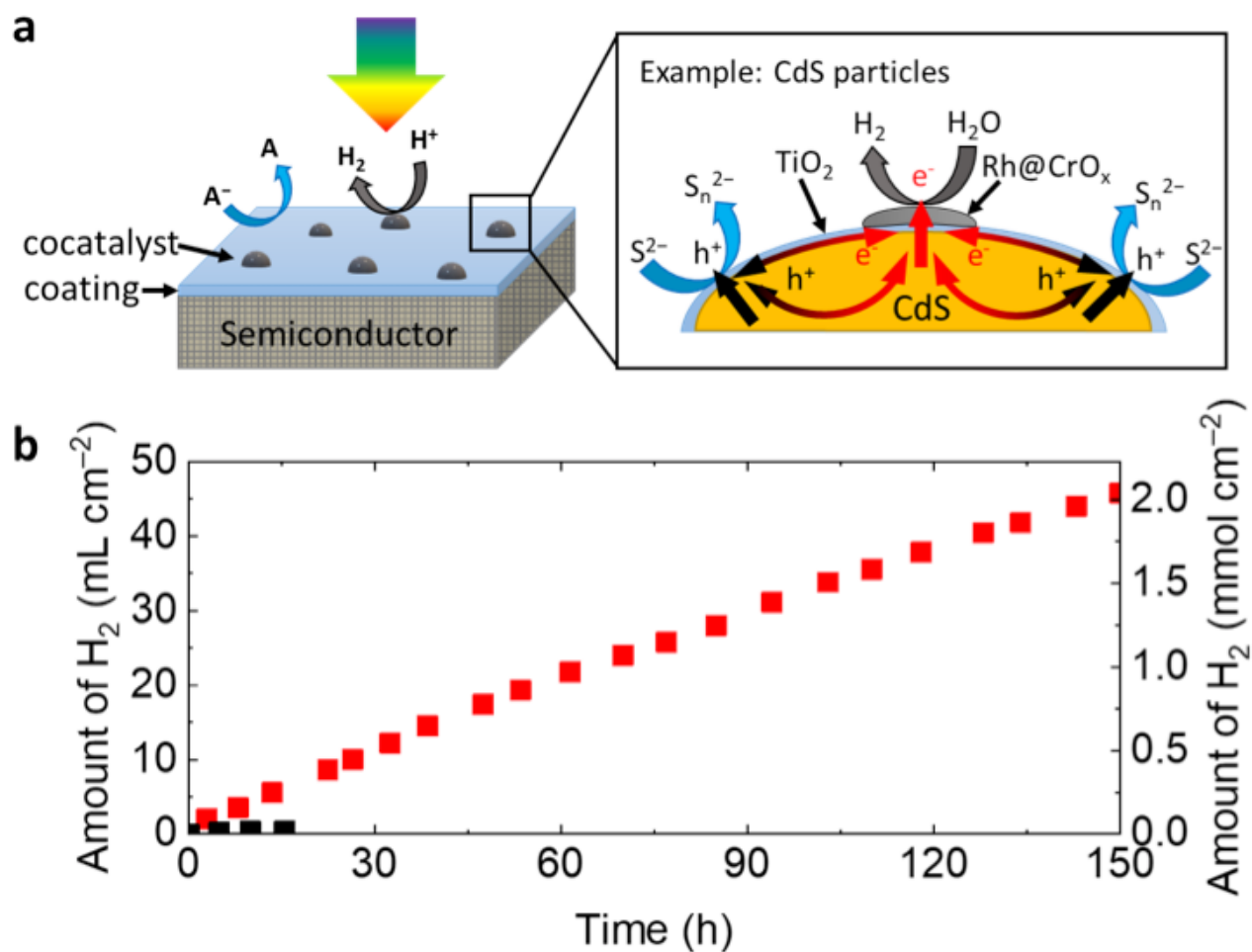


Figure 1

Coating-stabilised photocatalysts for coevolution reactions. a, Schematics of the coating-stabilised photocatalytic panel for coevolving H₂ and reversible redox couple A/A⁻. Inset: an example of the CdS/TiO₂/Rh@CrO_x photocatalyst, showing local charge flow directions in the CdS and injection of both electrons and holes at the coating-liquid interface. b, Continuous H₂ generation over 150 h by the CdS/3-nm TiO₂/Rh@CrO_x panel (red), compared to the ceased generation by the bare CdS panel without coatings and cocatalysts after 15 h (black).

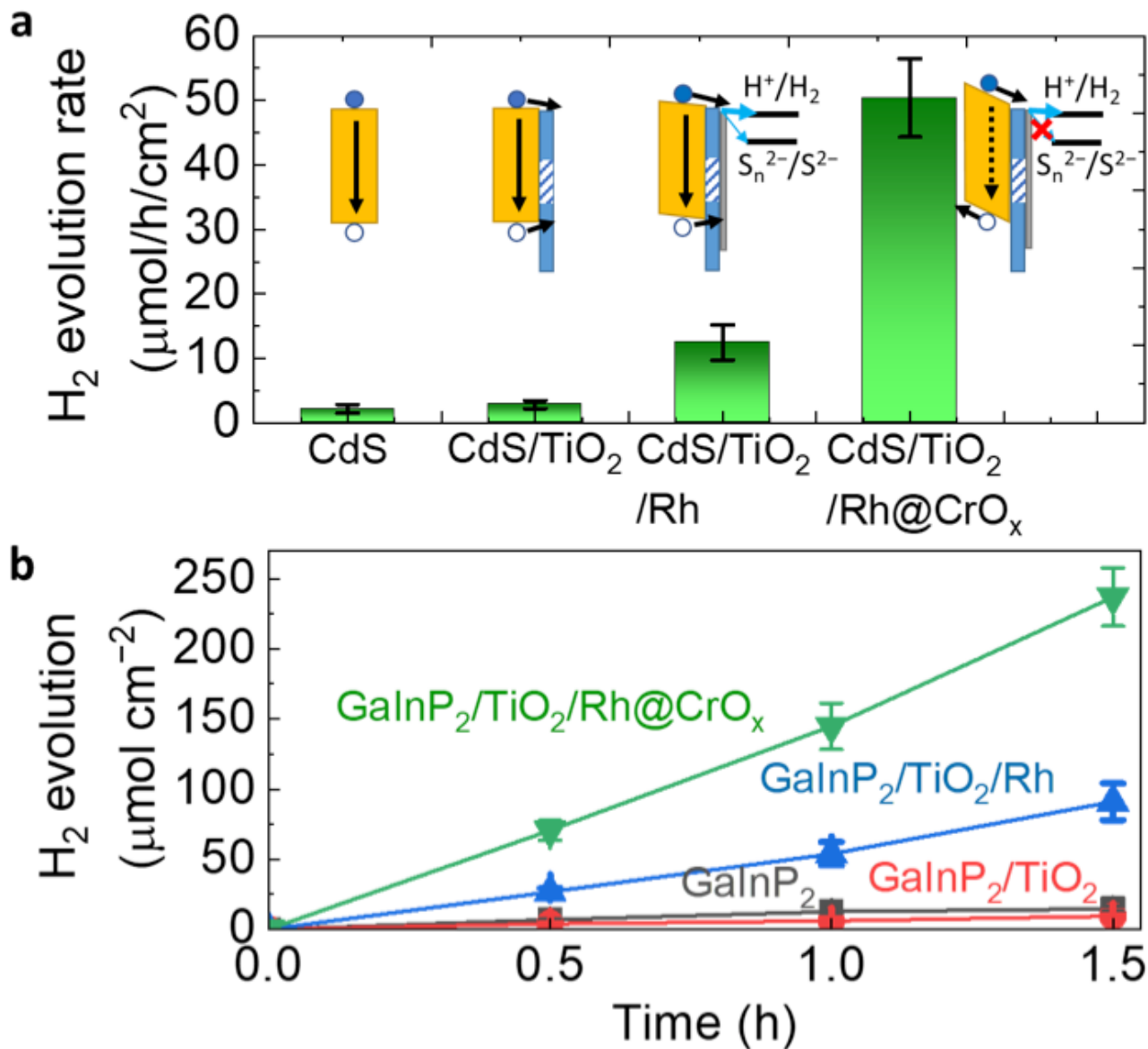


Figure 2

Charge separation of the photocatalytic panels. a, H₂-evolution rates of the CdS panel and b, time courses of H₂ evolution from GaInP₂ panels of bare surface, with 3-nm TiO₂ coating, with TiO₂/Rh, and with TiO₂/Rh@CrO_x in 100 mM Na₂S solutions (pH 13.5). Schematics in a, show the corresponding charge transport directions. The rate takes an average of at least three samples for each condition.

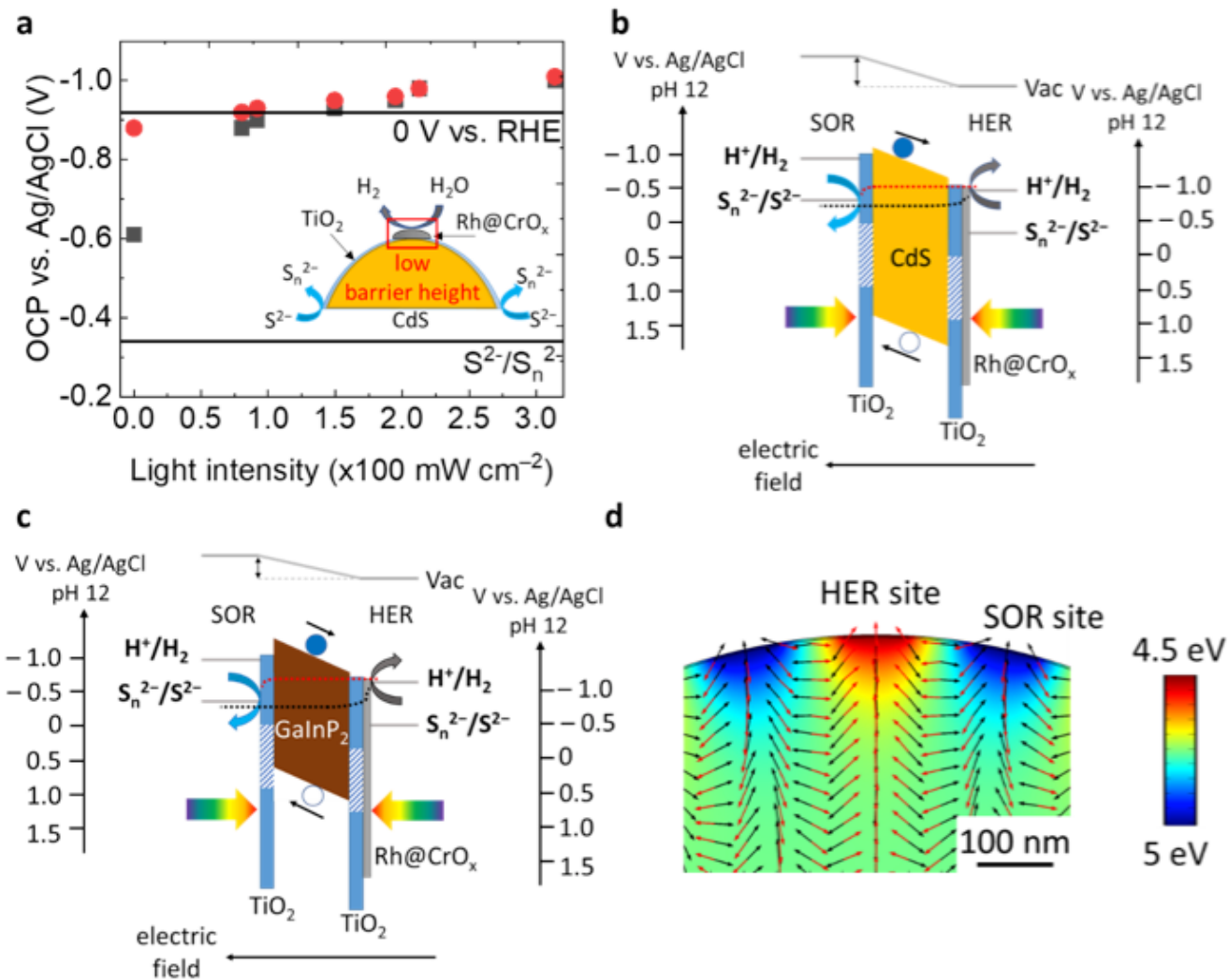


Figure 3

Local energetics of the photocatalytic panels. a, Light intensity-dependent OCPs of CdS/TiO₂/Rh@CrO_x particle-assembled photoelectrode in a 10 mM Na₂S aqueous solution without (black dots) and with (red dots) H₂ purging. Inset: Illustration of the low-barrier-height site at Rh@CrO_x. The OCP measured at 0 mW cm⁻² represents the dark condition, denoted as OCP_{dark}. Band diagram of the b, CdS and c, GaInP₂ photocatalyst between the SOR (left) and HER (right) sites are drawn along the liquid interface under illumination, but not into the semiconductor. Electron and hole quasi-Fermi levels are shown by the red and black dash lines, respectively. d, Simulated potential energy of the CdS CB edges. Black and red arrows represent the hole and electron transport directions, respectively.

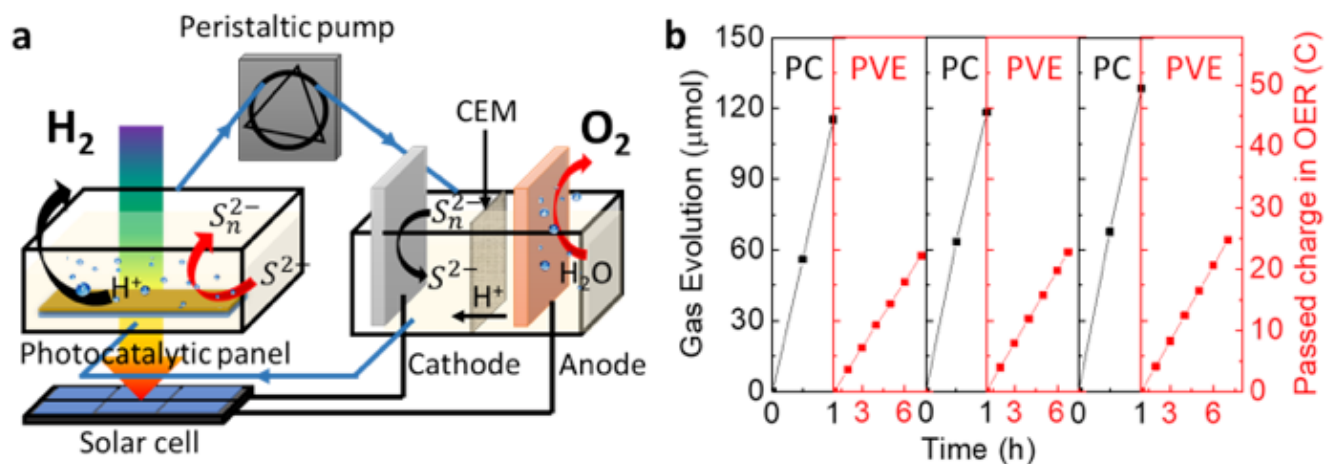


Figure 4

Redox-mediated water-splitting reactor. a, Schematics of the reactor, which is constructed by connecting a redox-mediated photocatalysis (PC) chamber with a photovoltaic-driven electrolysis (PVE) device. b, Stoichiometric amount of H_2 and O_2 evolved with STH 1.7% from the CdS panel during three cycles of alternating PC and PVE processes, respectively.

Supplementary Files

This is a list of supplementary files associated with this preprint. Click to download.

- [SupplementaryVideo1final.mp4](#)
- [SupplementaryVideo2final.mp4](#)
- [coatingstabilisedphotocatalystsSupportingInformation.docx](#)